Matter

CellPress
OPEN ACCESS

Article

# Innate immune cell instruction using micron-scale 3D objects of varied architecture and polymer chemistry: The ChemoArchiChip

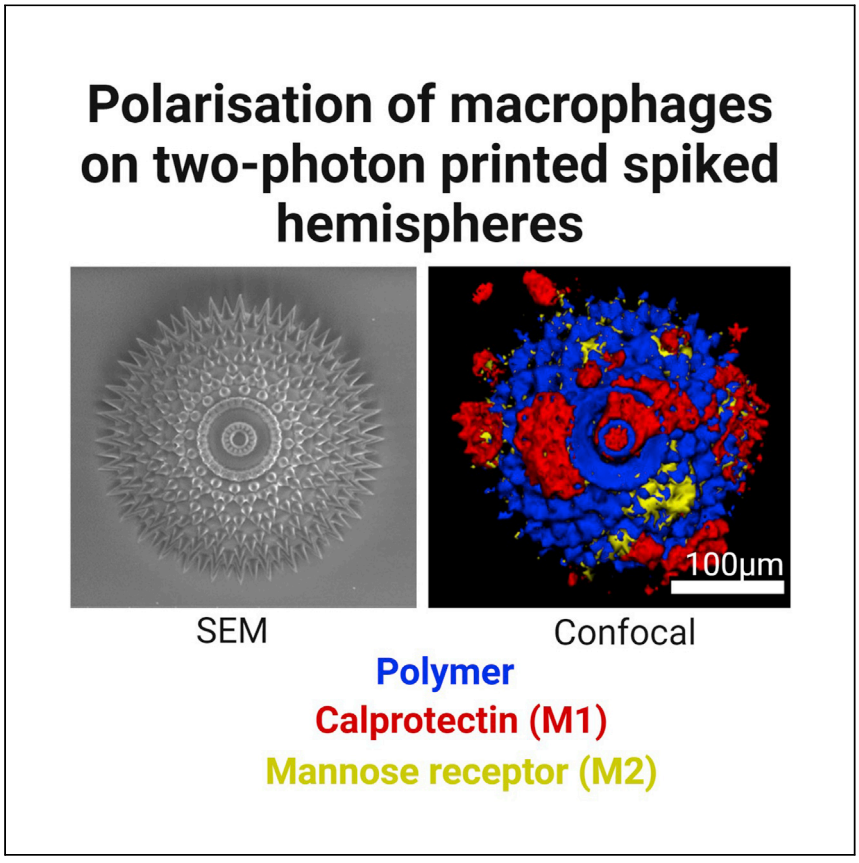


Matthew Vassey, Le Ma, Lisa Kämmerling, ..., Amir M. Ghaemmaghami, Ricky Wildman, Morgan R. Alexander

amir.ghaemmaghami@nottingham.ac.uk (A.M.G.)
ricky.wildman@nottingham.ac.uk (R.W.)
morgan.alexander@nottingham.ac.uk (M.R.A.)

## Highlights

*In vitro* screening gives design rules for cell response to geometries/chemistry

Object shape and vertex angle are drivers of macrophage attachment to 3D objects

Caveola-dependent endocytosis is mechanism for cell response to spiky objects

Implanted devices are essential components in medicine; e.g., hip replacements and coronary stents. The foreign body response to implants often results in implant encapsulation and persistent inflammation, a process that macrophage cells orchestrate. An array of complex geometries in combination with materials chemistry is screened, and putative design rules are identified to modulate macrophage attachment as well as macrophage differentiation toward pro- or anti-inflammatory phenotypes. Additionally, caveola-dependent endocytosis is identified as the principal mechanism for cell response to spiky objects.

1 **Discovery**
A new material or phenomena

Vassey et al., Matter 6, 887–906
March 1, 2023 
https://doi.org/10.1016/j.matt.2023.01.002

Matter

CellPress
OPEN ACCESS

Article

# Innate immune cell instruction using micron-scale 3D objects of varied architecture and polymer chemistry: The ChemoArchiChip

Matthew Vassey,[1,8] Le Ma,[2,6,8] Lisa Kämmerling,[1,8] Chidimma Mbadugha,[1] Gustavo F. Trindade,[2,6] Grazziela P. Figueredo,[3] Francesco Pappalardo,[6] Jason Hutchinson,[2] Robert Markus,[7] Seema Rajani,[7] Qin Hu,[2] David A. Winkler,[4,5] Derek J. Irvine,[2] Richard Hague,[2] Amir M. Ghaemmaghami,[1,*] Ricky Wildman,[2,*] and Morgan R. Alexander[6,*]

## SUMMARY

**To design effective immunomodulatory implants, innate immune cell interactions at the surface of biomaterials need to be controlled and understood. The architectural design freedom of two-photon polymerization is used to produce arrays of surface-mounted, geometrically diverse 3D polymer objects. This reveals the importance of the interplay between architecture and materials chemistry in determining human macrophage fate *in vitro*. The ChemoArchiChip identifies key structure-function relationships and design rules from machine learning models to build a mechanistic understanding of cell attachment and polarization. Object shape, vertex/cone angle, and size are key drivers of attachment. Particular shapes are found to heavily modulate pro- or anti-inflammatory cell polarization, while triangular pyramids drastically reduce or even eliminate attachment. Caveola-dependent endocytosis is a principal mechanism by which cells respond to objects with sharp points; i.e., low vertex/cone angles. The discovery of these putative design rules points to surfaces decorated with architectures to augment implant performance.**

## PROGRESS AND POTENTIAL

This study explores the design space made possible by two-photon polymerization to improve implant design; e.g. for hip replacements or coronary stents. To investigate the role of surface shape, we use two-photon polymerization to create an array of geometric and more complex 3D objects at a surface: the ChemoArchiChip. Two-photon polymerization allows fabrication of previously inaccessible geometries to identify key relationships between geometry/materials chemistry and macrophage behavior. The findings of this study and the discovery of putative design rules (identified in a training set and validated in a test set) for macrophage attachment and phenotype control by surface shapes paves the way for surfaces decorated with architectures to augment implant performance. This offers exciting possibilities to improve implant design for numerous medical implants.

## INTRODUCTION

Implanted devices are ubiquitous in healthcare, from coronary stents to hip replacements and glucose sensors to surgical meshes.[1–3] A major contributor to their significant failure rates is the foreign body response (FBR), often resulting in persistent inflammation and encapsulation of the device with a fibrous capsule, leading to its rejection.[4,5] To date, knowledge required for *a priori* design of low-FBR implants is absent. Systematic mapping of the critical relationships is needed to aid the design of these biomaterials.[6] Here we take a step toward this goal by developing an *in vitro* model capable of screening a large library of surface-mounted 3D objects formed from different polymer chemistries.

It is desirable to modulate the behavior and phenotype of macrophages because they are key regulators of the immune response to biomedical implants.[7–9] Macrophages exhibit a functional plasticity that plays a critical role in FBR-induced inflammation and subsequent tissue repair and regeneration.[10] It is now understood that many physical parameters affect the macrophage phenotype, simplified here as naive (M0), pro-inflammatory (M1), or anti-inflammatory (M2), with the last two

representing opposite ends of the macrophage polarization spectrum.[11,12] Implanted spheres have been shown to mediate macrophage responses and their ultimate success or failure *in vivo*,[13] with materials-induced cell shape changes modulating macrophage phenotype.[11,12,14–16] Independently, recognition that the materials chemistry can also direct immune responses has led to a range of materials-based strategies. Early approaches have attempted to dampen undesirable immune responses by creating surfaces that resist non-specific protein adsorption,[17] create entropic barriers to adsorption,[18] mimic cell membranes,[19] or build super-hydrophilic barriers to fouling.[20] More recent approaches have attempted to steer immune responses by conjugating materials with immune-stimulatory enzymes[21] or using high-throughput screening methods to identify materials that reduce the FBR in murine models and non-human primates[22,23] or that modulate immune cell-instructive responses *in vitro* and in murine models.[15]

Here, we go beyond these approaches to elucidate how macrophages respond to a range of surface-mounted micro-scale objects composed of three immune-instructive polymer chemistries. These are constructed using advanced additive manufacturing that combines materials chemistry and 3D architectural cues. Two-photon polymerization was used to create an array of complex objects (the ChemoArchiChip) with critical dimensions in the range of 5–120 μm, allowing us to efficiently explore the role of object architecture and materials chemistry in directing macrophage behavior.[22–28] We found that macrophage attachment and phenotype can be tuned via highly specific combinations of size, geometry, and material. We show that vertex angles must be less than 60° to induce significant macrophage attachment to an object and that some objects, such as tetrahedra, can drastically reduce or even eliminate attachment depending on their size. The primary mechanism governing these interactions is found to be caveola-dependent endocytosis. Interestingly, for macrophage polarization, material chemistry dominates architecture, but it can be tuned using an appropriate choice of shape to elicit strong cell responses.

## RESULTS

### Design and fabrication of the ChemoArchiChip

To create structures of relevance to macrophage instruction, photocurable monomers were selected for manufacture with two-photon polymerization (2PP) (Figure 1A; supplemental experimental procedures) using a high-throughput screen of flat homopolymers in micro-array format that identified polymers modulating the macrophage phenotype (Figure S1). Those identified to modulate the macrophage phenotype for 2PP were derived from the following monomers: BDDA (1,4 butanediol diacrylate), M1; polymer GPOTA (glycerol propoxylate triacrylate), M0; and polymer GDGDA (glycerol 1,3-diglycerolate diacrylate), M2. Through a chemically informative model, the polymers' molecular fragments were investigated, and specific molecular features that contribute most to the classification of polymers as either M1 or M2 polarizing were identified (Figure S1B).[29] Molecular fragments mostly associated with polymers inducing high M2/M1 ratios were CO, C(C), and C(CN) (Figures S1C and S1D). These base monomers were reformulated, where necessary, with pentaerythritol triacrylate (PETA), along with a print optimization procedure to achieve reliable fidelity (Figures S2 and S3). This resulted in three formulations consisting of GPOTA (M0), a blend of BDDA and PETA (60:40 [w/w]) referred to as BDDA (M1), and a blend of GDGDA and PETA (80:20 [w/w]) referred to as GDGDA (M2) (Figure S4). The surface chemistry was confirmed to match that of the intended monomers using time-of-flight secondary ion mass spectrometry

[1]Immunology & Immuno-bioengineering Group, School of Life Sciences, University of Nottingham, Nottingham NG7 2RD, UK

[2]Faculty of Engineering, University of Nottingham, Nottingham NG7 2RD, UK

[3]School of Computer Science, University of Nottingham, University Park, Nottingham NG8 1BB, UK

[4]Department of Biochemistry and Chemistry, La Trobe Institute for Molecular Science, La Trobe University, Bundoora, VIC 3042, Australia

[5]Monash Institute of Pharmaceutical Sciences, Monash University, Parkville, VIC 3052, Australia

[6]School of Pharmacy, University of Nottingham, Nottingham NG7 2RD, UK

[7]School of Life Sciences Imaging (SLIM), University of Nottingham, Nottingham NG7 2RD, UK

[8]These authors contributed equally

*Correspondence: amir.ghaemmaghami@nottingham.ac.uk (A.M.G.), ricky.wildman@nottingham.ac.uk (R.W.), morgan.alexander@nottingham.ac.uk (M.R.A.)

https://doi.org/10.1016/j.matt.2023.01.002

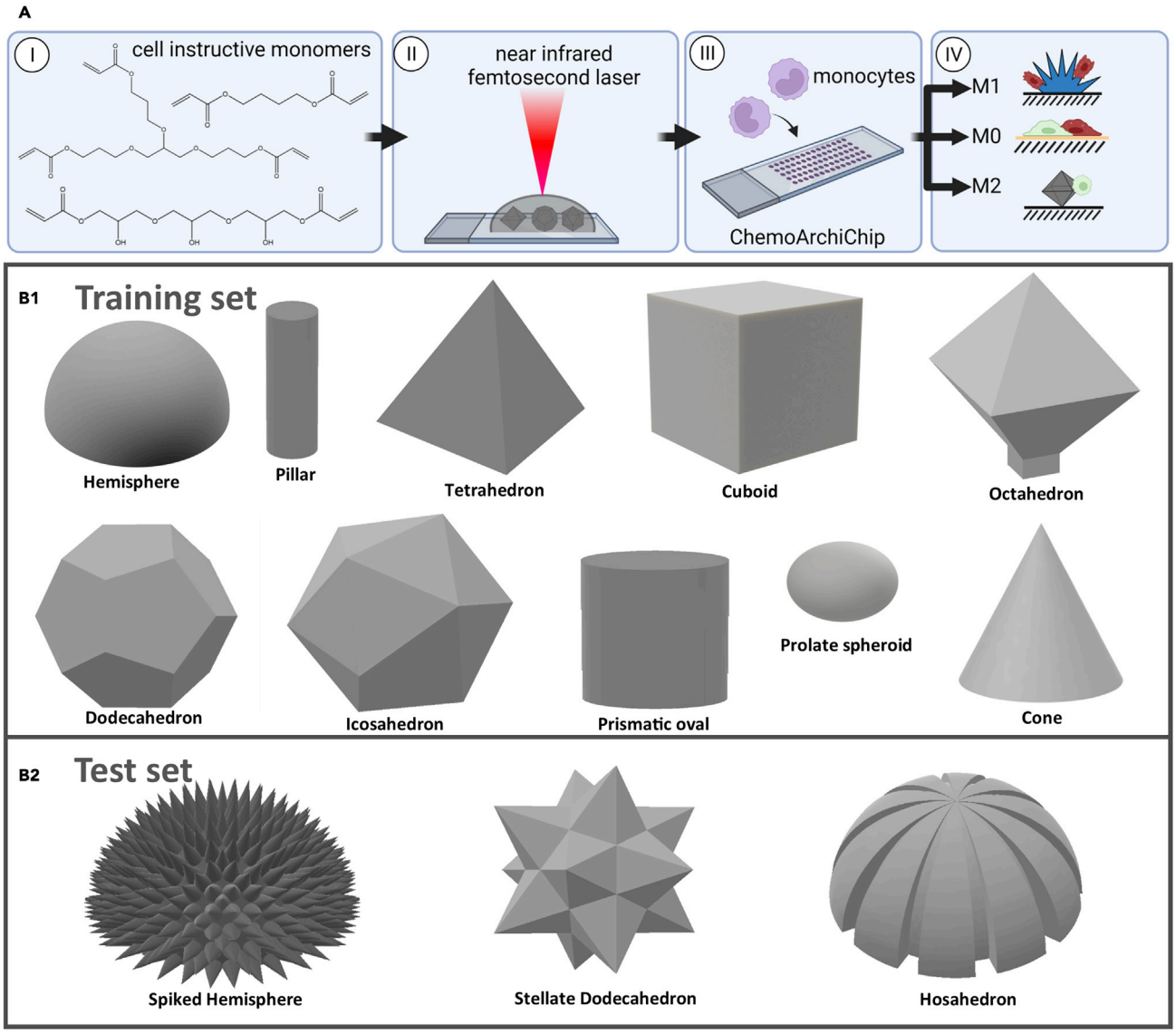


**Figure 1. Design and fabrication of the ChemoArchiChip**

(A) Schematic of the screening process. I: materials selection. II: additive manufacture. III: cell seeding. IV: biofunctional assay.

(B) Schematic object overview of training (B1) and test set (B2) for the ChemoArchiChip screening. In a first library of objects, the training set comprised hemispheres; pillars; tetrahedra; cuboids; octa-, dodeca-, and icosahedra; prismatic ovals; prolate spheroids; and cones to systematically change simple parameters of their geometries. Findings related to cell attachment were tested on spiked hemispheres, stellate dodecahedra, and hosohedra.

(Figure S5). The addition of PETA as a minor component was not observed to have a significant effect on macrophage polarization (Figure S4C). Raman spectra showed a high level of conversion consistent with full polymerization of di- and tri-acrylate monomers (Figure S6). Atomic force microscopy (AFM) experiments additionally determined a similar wet surface modulus for GPOTA (M0) and GDGDA (M2) but with BDDA (M1) being stiffer (Figure S7).

## Macrophage attachment to 3D objects

Topographical modulation of macrophage behavior is well established on flat surfaces[12,24,25] and for spherical and ellipsoid particles.[13,16,26] To determine the effect of specific 3D objects on a surface, we performed a systematic study of the design

space using mathematically describable geometries in a training set, generating a rich dataset from which relationships can be mined. In this training set we used simple polyhedra (cubes; pillars; icosa-, dodeca-, octa-, and tetrahedra; and hemispheres) and other shapes, including prismatic ovals, cones, and, prolate spheres (Figures 1B and S8–S10). We then varied parameters that determine the object shape and size, including heights, base diameters and side lengths, aspect ratios, and vertex angles. The vertex angle (also known as the polyhedral angle) is defined as the angle at the point where two or more lines, curves, or edges meet, which vary in polygons because of their number of edges (n) and can be varied using the dimensions of the objects; for example, the height of the tetrahedron of a given base size can be increased to decrease the vertex angle for a given height object. The dihedral angle is the angle between two faces. Using the control afforded by the 2PP fabrication process, we were able to explore the influence of changes engineered in the object architecture for a training set consisting of polyhedra, cones, prismatic ovals, and prolate spheres (Figure 1B).

## The importance of aspect ratio and vertices in controlling macrophage attachment

The cell response to this library of objects was examined by culturing human monocytes on ChemoArchiChips for 6 days, measuring their attachment to objects, and classifying the monocyte differentiation into macrophages by their polarization state. Automated confocal z stack image acquisition and 3D image analysis protocols were developed to identify and count the cells in contact with the objects. These were expressed as attachment (cell number per object)/area. The robustness of donor-donor responses was tested via correlation of attachment data across all 5 donors, showing a minimum $r$ value of 0.87 (Figure S14), with flat printed areas for all donors showing similar levels of attachment (Figure S15).

The cell attachment for 3D objects was rank ordered for GDGDA attachment for the different materials chemistries. This showed that the order of object modulation of cell attachment by their architecture was similar but not identical for each polymer. GDGDA had a higher macrophage attachment to objects than GPOTA and BDDA, which were very similar (Figure 2A). For pillars, the circularity of a series of prismatic ovals was systematically varied from circular to oval at a fixed pillar height (30 μm). Cell attachment increased as the object became less circular and as the object minor axis diameter decreased from 80 μm to 10 μm (Figure 2C). The engineering of such subtle differences and observing their effect on macrophages has not been possible for 3D objects prior to two-photon printing.

Cell attachment was greatest for octahedra and hemispheres (all 15 μm diameter; Figure 2D). For all polymers, octahedra exhibited significantly greater attachment than the flat controls and the other objects. The hemisphere exhibited the second highest attachment (Figures 2D and 2E). A plot of macrophage attachment against object base diameter for all polyhedra revealed a preference for smaller objects (Figure 2F).

We hypothesized that the vertex angle of surface-bound objects could influence macrophage attachment as they attempt to engulf them.[16] We first tested this by examination of the vertex angle for the array of polyhedra as well as the cone angle of the cones (Figures 2D and 2E; Table S3). Examining the attachment data for samples with polyhedral and cone samples included in Figure 3A indicates that objects with vertex/cone angles below 60° (more pointed) showed significantly higher cell attachment than objects with vertex/cone angles above 60°. A large range of

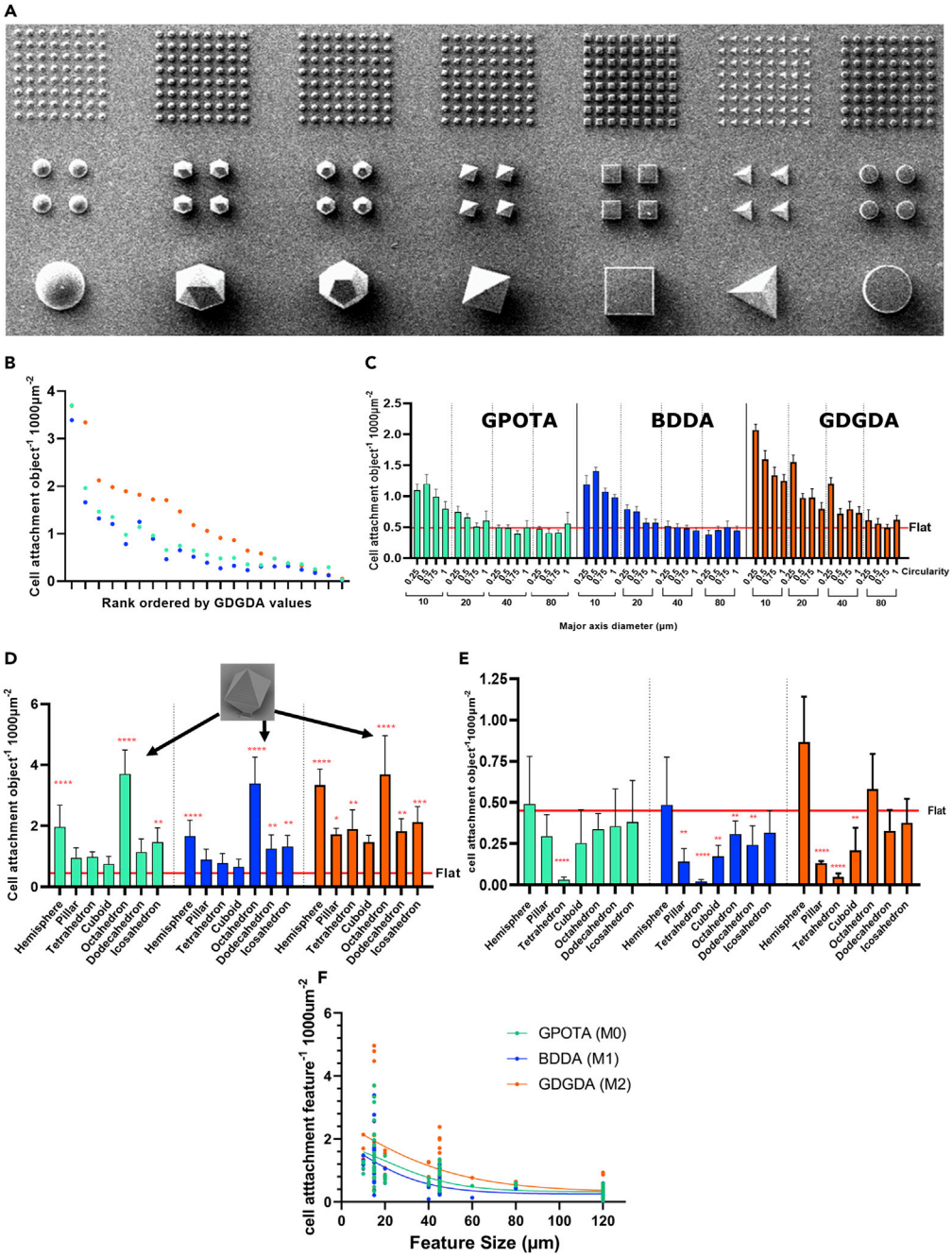


**Figure 2. Training set of polyhedra give insights into cell attachment**

(A) Representative SEM images of polyhedra (in three different sizes: 120-, 45-, and 15-µm diameter; top, center, and bottom panel, respectively) evaluated for cell attachment (left to right: cylinder, tetrahedron, cube, octahedron, dodecahedron, icosahedron, and hemisphere).

(B) Attachment performance rank order of mean macrophage attachment (per object and ordered from largest to smallest GDGDA attachment) of polyhedra shown in (A) was calculated to compare object performance across different chemistries.

(C) Bar charts of macrophage attachment to prismatic ovals (used to investigate aspect ratio). Data are expressed as mean (±SD) number of cells per unit area (µm$^2$ × 1,000) of each object. Only cells associated with 3D objects were quantified using segmentation of fluorescence data (experimental procedures). Green bars represent GPOTA (M0), blue bars represent BDDA (M1), and orange bars represent GDGDA (M2) substrate materials.

(D and E) Bar chart of macrophage attachment to polyhedra (object diameter = 15 µm, D; object diameter = 120 µm, E). Inset: SEM image of the octahedron from the top. The solid horizontal line indicates the attachment of the flat, planar area. Data represent 5 biologically independent donors and a total of 9 technical repeats (****p < 0.0001, ***p < 0.001, **p < 0.01, *p <0.05).

(F) Macrophage attachment per object versus the object size descriptor for each material and all objects; a non-linear best fit curve was fitted.

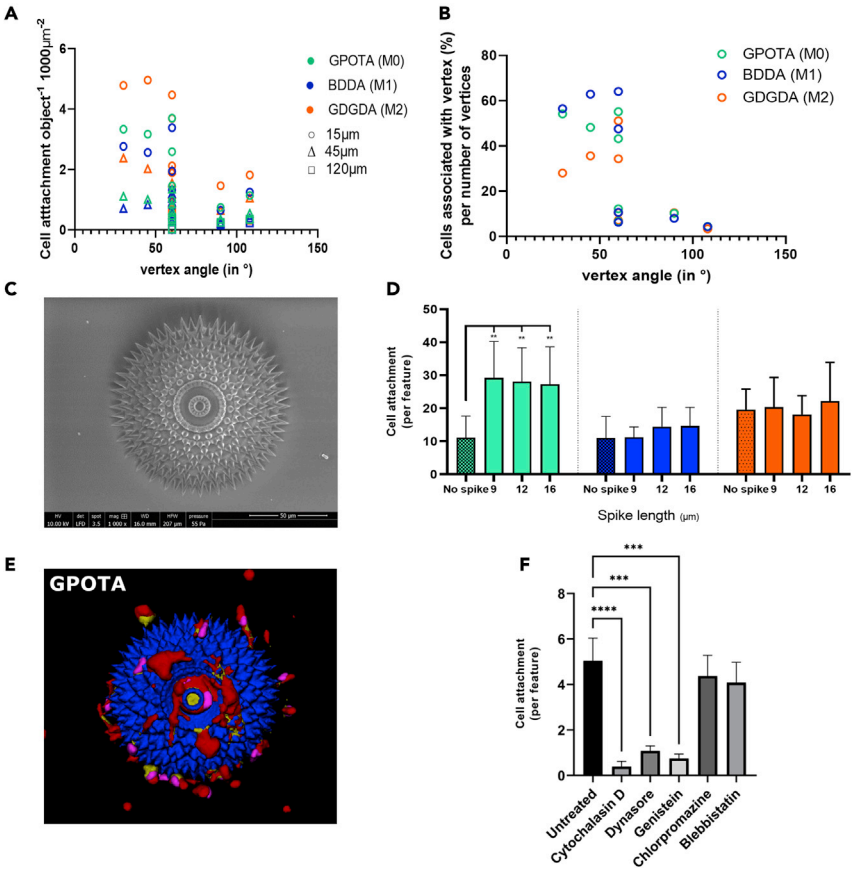


**Figure 3. The role of micro-sized objects on surfaces in controlling macrophage attachment**

(A and B) Surface area-normalized cell attachment versus vertex/cone angles, separated by material and base diameter of all polyhedra/cones (A), and percentage of cells associated with vertices per number of vertices versus vertex/cone angle of polyhedra and cones (B). Data are expressed as mean number of cells per unit area for each individual object (only cells associated with 3D objects were quantified). Green bars represent GPOTA (M0), blue bars represent BDDA (M1), and orange bars represent GDGDA (M2) substrate materials.

(C and D) SEM image of a GPOTA-spiked hemisphere (base diameter, 120 µm; spike length, 9 µm) (C) and quantification of cell attachment (D) according to (E). "No spike" indicates a smooth hemisphere. Data represent 5 biologically independent donors and a total of 9 technical repeats.

(E and F) Confocal images represented as a 3D rendering of a GPOTA-spiked hemisphere (base diameter, 120 µm; spike length, 9 µm) with object in blue, macrophage nuclei in magenta, macrophages expressing calprotectin (an M1 marker) in red, and mannose receptor (an M2 marker) in yellow (E) and elucidation of the mechanism of macrophage attachment to spiked GPOTA hemispheres (F). Macrophages were pre-treated with the indicated inhibitors for 0.5 h and then cultured on surfaces for a further 72 h. Bars indicate mean (±SD) of cell attachment per individual objects. Data represents 4 biologically independent donors (with a minimum of 4 technical repeats per donor) (****$p < 0.0001$, ***$p < 0.001$, **$p < 0.01$).

attachment was observed at a vertex/cone angle of 60°. By examining the cell positions in the microscopy data, we also noted that cells preferred vertices to faces, with up to 70% of the cells observed to be located on the vertices in some cases (Figure 3B). This critical angle is similar to the findings of Champion and Mitragotri,[16] who determined 45° as a threshold for phagocytosis of ellipsoid microparticles.

Interestingly, our largest tetrahedra (with 120-µm base diameter) with only one vertex (angle 60°) had zero cell attachment for all polymers (Figure 2E), although the effect was not seen for the 45-µm version of these triangular pyramids (Figure S8I). This

is consistent with the general trend of smaller objects encouraging attachment (Figure 2F). Tetrahedron-decorated surfaces might therefore be a way of reducing macrophage attachment for implants. Hemispheres had levels of attachment similar to the flat surface controls for all three polymers, suggesting that macrophages were not sensing the hemisphere at the scales employed. Attachment to prolate spheres with varying base diameters and increasing heights was higher for the smaller sizes, while larger objects had levels of attachment similar to the flat surfaces (Figure S10).

Cones showed significantly higher attachment than the flat surface controls for all polymers, and cones with a 15-μm base diameter had higher attachment than the 45-μm diameter cones. A significant reduction in attachment was observed with increasing cone angle, consistent with the behavior of the tetrahedra and attachment to vertex angles (Figures 3A and S10A). Attachment was not entirely eliminated, most likely because of the smaller size of the cones relative to the 120-μm base tetrahedra.

### Macrophage attachment to more complex 3D objects

We tested the observations from the training set with more complex architectures (Figure 2B). The identification of the importance of high-aspect-ratio objects, such as cones and prismatic ovals, prompted us to investigate the effect of addition of spikes to hemispheres that already exhibit high cell attachment. We developed a range of spiked hemispheres with different base diameters and spike lengths attached to the surface (Figure S13). Confocal microscopy revealed intimate macrophage attachment to the spike tips with significant cytoskeletal changes and remodeling of the cell membrane to conform to the structures (Figure S13F). The presence of spikes on the surface increased cell attachment per unit area 3-fold compared with a smooth hemisphere for GPOTA (M0) (Figure 3D). The length of the spikes tested did not influence attachment, suggesting that the tip of the spike (or vertex) itself was the most important attribute for increasing attachment (Figure 3D). This is consistent with the importance of vertices in influencing macrophage attachment, as noted above.

Spheres were printed with grooves (hosohedra) to test whether cell confinement and contact guidance observations on flat substrates would translate to 3D striated objects The number of grooves (0–14 10-μm grooves per structure) in a 3D hemispherical hosohedron was sequentially increased across an array of hemispheres, and their macrophage attachment was assessed. The presence of grooves in these objects did not increase cell attachment for the GPOTA (M0) and BDDA (M1) polymers but did so for GDGDA (M2) hosohedra (Figure S11). Notably, in contrast to literature reports of 2D grooves, we did not observe contact guidance along our grooved hemispheres (Figure S11B).[12,25,27,28] This suggests that macrophage spreading and attachment behave differentially in 2D and 3D. While macrophages align themselves along grooves in 2D, this is not the case for grooves on 3D curved objects, such as hosohedra.[30] Consistent with findings for the other objects, for stellate dodecahedra, attachment is progressively smaller when object size increases from 15 μm to 45 μm and 120 μm (Figure S12).

Machine learning was used to search for relationships between macrophage attachment and quantitative descriptors of the objects listed in Table S1. The descriptors encoded the geometric properties of the objects, such as the surface area, volume, or linear dimensions, but also quantified the sub-elements used to construct the objects (defined here as primitives); e.g., number of cylinders or spikes. A linear regression model was generated (Figure S14) that revealed the importance of having large numbers of small objects per array, larger vertex angles, as well as larger object

voxel volume for increasing cell attachment. The performance of the linear regression model for macrophage attachment is shown in Figure S14. Strong correlations between the linear model predictions compared with the measured values in the test sets, with average $R^2$ of 0.80 $\pm$ 0.03 and root-mean-square error (RMSE) of 0.02 $\pm$ 0.003 (Figures S14A and S14B). More space between spikes (indicating fewer numbers of spikes on objects) and larger vertex angles were found to have a negative influence on macrophage attachment (Table S1). The model was also consistent with visual observations of GDGDA increasing macrophage attachment (Figure S14).

### Inhibition of phagocytic pathways to determine attachment mechanism

Given that the attempt to phagocytose structures appears likely to be responsible for macrophage interactions with objects, a range of inhibitors were employed that interfere selectively with specific endocytosis and phagocytosis pathways. This would elucidate the underlying attachment mechanisms for GPOTA (M0) that support the M0 macrophage phenotype and exhibit large differences in macrophage attachment depending on whether the hemispheres had added spikes. Macrophage attachment to spiked hemispheres was abolished with addition of cytochalasin-D, dynasore, and genistein (Figures 3F and S16). Similarly, loss of cell attachment was also observed on octahedra, stellate dodecahedra, cones, and prismatic ovals (Figure S16). Experiments showed that decreased cell attachment was not due to diminished cell viability and that the inhibitors used did not interfere with macrophage attachment on flat tissue culture plastic surfaces (TCP) (Figures S17–S20). The inhibition of cell attachment by genistein suggests caveola-dependent endocytosis. This is directly mediated in two ways: preventing actin depolymerization in the local cortical cytoskeleton (inhibited by cytochalasin-D) and recruitment of dynamin (inhibited by dynasore). Chlorpromazine, which inhibits clathrin-dependent pathways, and blebbistatin, which inhibits myosin II and frustrated phagocytosis, had no effect on cell attachment. This provided additional support for macrophage phagocytic behavior being responsible for the significantly increased attachment to spikes as macrophages attempt to engulf these objects (Figure 3F).[16,31–33] Prior work on caveola-mediated endocytosis in nanostructures has described how high-aspect nanostructures can locally deform the cell membrane, leading to accumulation of intracellular scaffolding proteins and initiation of endocytosis.[34,35] Similarly, it is understood that the addition of spikes with vertices resembling nanopillars will lead to membrane deformation phagocytosis driven attachment.[36,37]

### Macrophage polarization: Combinatorial role of 3D object shape and materials chemistry

Having identified several key object shapes that modulate cell attachment, we wanted to understand their effect on macrophage phenotype. A key process in maintaining tissue homeostasis is the macrophage polarization state, which is an important determinant of clinical outcome following medical device implantation. Previous studies have shown how macrophage polarity can be modulated by chemistry or topography. By utilizing the design freedom and throughput of two-photon printing, we aimed to increase our understanding of possible synergistic roles of object shape and substrate chemistry in this biological process.

Monocytes were cultured for 6 days, and phenotypic status was established using cell surface markers known to be associated with M1 and M2 phenotypes (calprotectin and mannose receptor for M1 and M2, respectively).[15,38,39] To estimate phenotypic responses, the M2/M1 marker expression ratio was calculated for all cells in direct surface contact with printed objects.

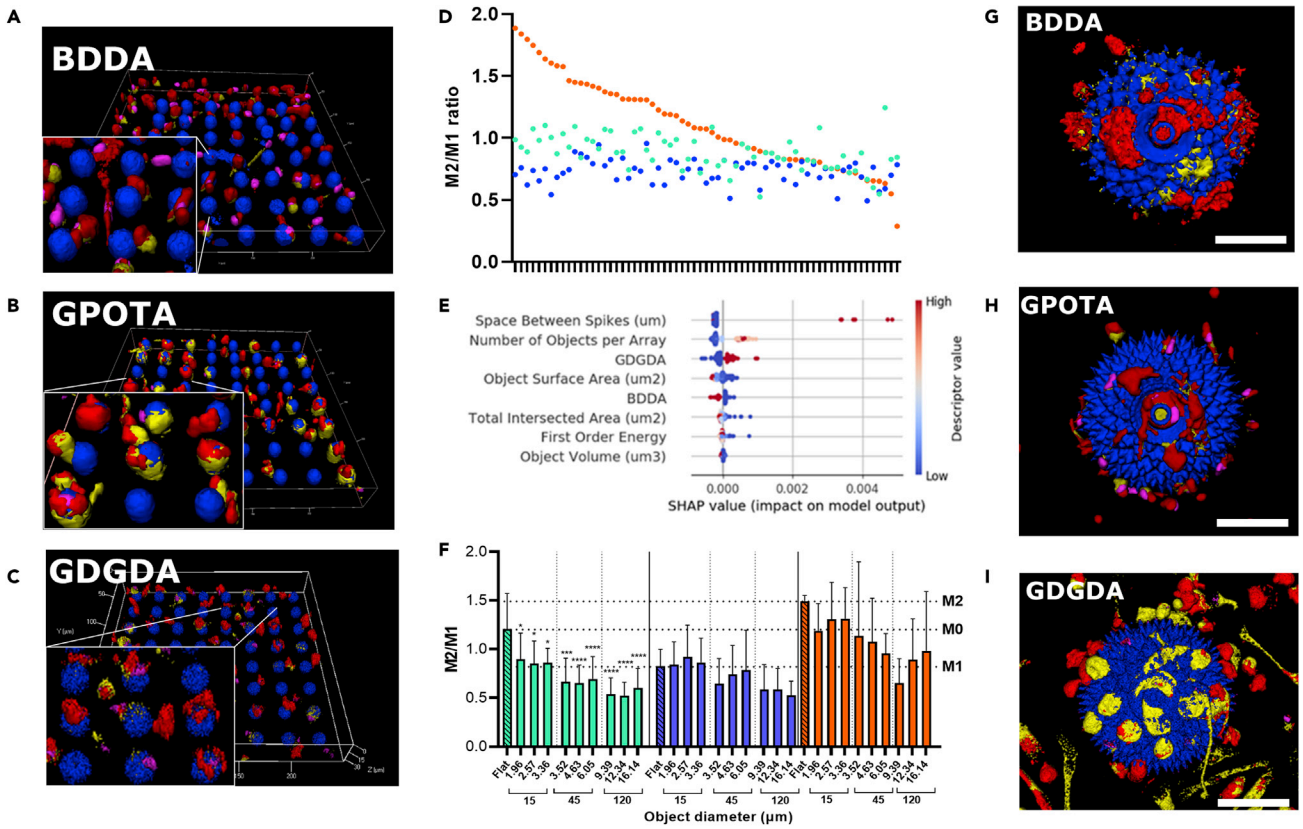


**Figure 4. Controlling macrophage phenotype using 3D object and surface chemistry**

The polarization status of macrophages cultured on ChemoArchiChips for 6 days was quantified using surface markers.

(A–C) 3D view of prolate spheroids (blue autofluoresence) with magnified 3 × 3 area (object diameter, 15 μm; height, 15 μm) composed of BDDA, GPOTA, and GDGDA respectively, with macrophages expressing calprotectin (an M1 marker, red) and mannose receptor (an M2 marker, yellow).

(D) The phenotype performance rank order of mean M2/M1 ratio (per object and ordered from largest to smallest GDGDA M2/M1 ratio) was calculated to compare object performance across different chemistries.

(E) Rank-order SHAP analysis of descriptors that mostly affect changes in macrophage phenotype on all substrates. Red points represent high data values for the descriptor. Blue dots represent low data values. SHAP values greater than 0 mean positive impact and less than 0 negative impact.

(F) Polarization state of macrophages cultured on spiked hemispheres. Data expressed as M2/M1 ratio were determined from mean cell fluorescence intensity per cell (±SD). Only cells associated with 3D objects were quantified. N = 5 biologically independent donors. A hatched bar indicates the flat planar area on the array, and the horizontal line indicates the value for exogenous cytokine polarization carried out in parallel.

(G–I) Top-down view of spiked hemispheres with macrophages expressing calprotectin (an M1 marker, red) and mannose receptor (an M2 marker, yellow). Scale bar, 100 μm. *p < 0.05, **p < 0.01, ***p < 0.001, ****p < 0.0001.

Culture of macrophages on different material substrates elicited different phenotypic responses, exemplified for prolate spheres in Figures 4A–4C and S22. Rank order analysis of M2/M1 ratios demonstrates the range of macrophage phenotypes achieved on the ChemoArchiChip (Figure 4D). A non-linear extreme gradient boosting machine learning method employing 1-hot descriptors for materials identity (Figure 4E) had an $R^2$ of 0.98 and 0.93 for the phenotype training and test sets, respectively (Figure S20). There were no strong linear relationships for the polarization for the composite polarization variable log(M2/M1) × attachment.

Shapley additive explanations (SHAP), a model-agnostic feature importance approach based on game theory, was used to quantify descriptor importance for a specific prediction. SHAP values indicate the relative importance of object descriptors that drive macrophage phenotype. SHAP values are calculated for each individual prediction and do not provide global information about a model.[40] SHAP value

descriptors are generated by comparing model predictions when the feature is present and absent. This is done for all possible subsets of all features that do and do not contain the feature of interest. This shows that, while the space between spikes, numbers of object per array, and object surface area are important, phenotype is mainly driven by chemistry (Figure 4E). This is indicated by clear separation between low and high descriptor importance values for GDGDA and BDDA, whereas other object features did not separate as much.[40] The ranges of SHAP values arise because, for non-linear models, feature importance is not constant throughout the model as in linear models, and rather depends on where it is assessed. Cytokine-polarized macrophages were used as controls (Figure S21).

On flat planar surfaces, we observed a significant decrease in M2/M1 ratio for cells cultured on BDDA (M1), indicating an increase in an M1 phenotype compared with GPOTA (M0). GDGDA (M2) had an increased M2/M1 ratio, indicating an anti-inflammatory phenotype (Figure S22). For 3D objects fabricated from BDDA (M1), we noted no change in cell phenotype compared with the flat control, suggesting that the surface chemistry is the dominant driver in cell phenotype control (Figure S22). However, for the GPOTA (M0) substrate, we noted a range of polarization for different objects and geometries, allowing a regression model to be derived that described the geometry-polarization relationship.

Macrophages cultured on spiked hemispheres created from all 3 polymer types had reduced M2/M1 ratios equivalent to an increased inflammatory phenotype compared with cytokine-polarized controls (Figure S21). GPOTA (M0) and BDDA (M1) had levels comparable with the M1 phenotype, and GDGDA (M2) had levels comparable with M0-phenotypes (Figures 4F–4I). The role of spikes in driving inflammatory responses has been reported previously for titanium particles.[33] Given the mechanosensitive activation by spiked microparticles, we hypothesize that there is potential overlap in the mechanisms driving inflammatory processes activated by spikes on solid substrates also, which is further supported by our findings of preferential macrophage attachment to objects with smaller vertex angles.

## DISCUSSION

It is possible to extract putative design rules for immune instruction using surface architecture and materials chemistry from this rich dataset (see schematic in Figure 5). Reducing the size of objects generally results in an increase in cell attachment (Figure 2F). This is supported by the machine learning model where small objects are highlighted to positive drivers of attachment. This is consistent with previous reports of macrophage attempted phagocytosis of particles in suspension and their attachment to supported 2D topographies.[13,14] Increased attachment to high-aspect-ratio objects is consistent with earlier studies of free-floating particles[26] that indicated that the angle of the tangent to the particle surface at the cell-material interface is key to the phagocytic outcome. Attachment was also found to be strongly dependent on vertex/cone angle, with 60° representing the threshold below which macrophage attachment significantly increased (Figure 3A). This has parallels in observations of attempted phagocytosis of particles where a study of polystyrene ellipsoids revealed a critical angle in that context.[16] Internalization only occurred when macrophages attempted to phagocytose particles that were spheres or when they approached elliptical spheroids end on; other approach directions or greater angles resulted only in spreading. While the observed attachment is very different from internalization of a particle, we view the coincidence of a critical angle below which the cell response changes as being significant; hence, critical angles

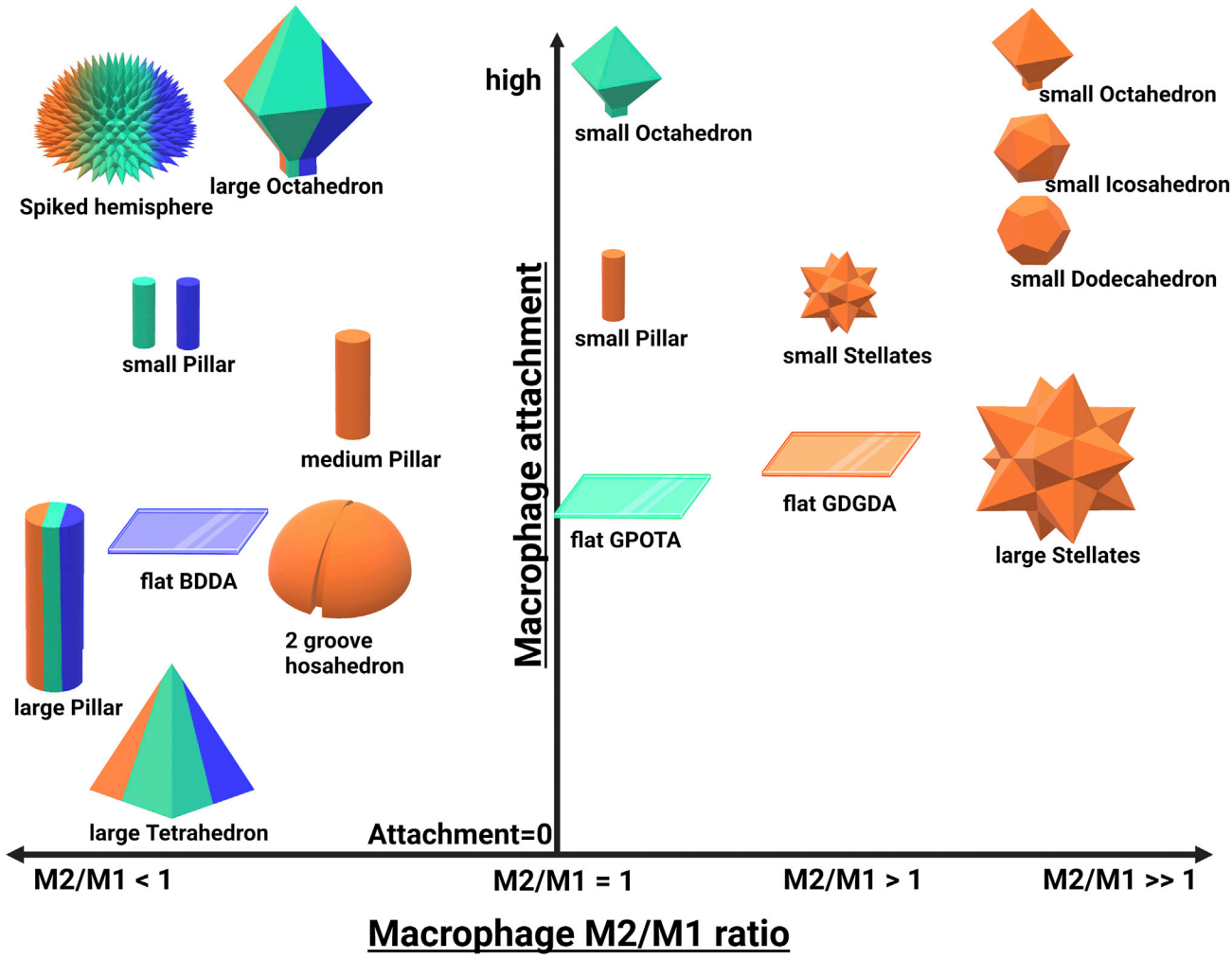


**Figure 5. Design rules gained from the ChemoArchiChip**

Schematic summarizing the design map for surface architecture- and material chemistry-driven macrophage attachment and phenotype. The figure shows representative shaped objects, classified and shown as large, medium, or small, and denoted by four possible colors, where green represents GPOTA (M0), blue represents BDDA (M1), and orange represents GDGDA (M2) substrate materials, and use of all three colors indicates that all of the three explored materials express the same behavior.

(vertex angle and cone angle) are seen arising for particle engulfment and for attachment to larger objects.

For objects with vertex angles below 60°, most cells on objects were associated with vertices (Figure 3B). The favored adherence to vertices can additionally be linked to phagocytosis-driven attachment because vertices will deform the membrane in a similar way to when they encounter microbes or high-aspect nanostructures.[26,36,37] In the case of tetrahedra, it appears that it is the specific vertex angle (and the low number of vertices) combined with larger object size that plays a role in significantly reducing cell attachment to this object.

Previously it has been found that different chemistries adsorb proteins differentially in quantity and identity, with protein adsorption identified as a prime driver of macrophage polarization.[15] At the same time, it has been found that chemistry has a greater influence over macrophage polarization and that topographical shape

can have synergistic/agonistic effects on polarization.[41] This can be seen here with GDGDA (M2) because differential polarization was observed depending on the specific architecture they were cultured on. Most objects induced an M0 or M1 phenotype, while fewer objects drive the M2 phenotype. Specifically, small polyhedra and small prolate spheres constructed from GDGDA (M2) as well as large stellates exhibited increased M2/M1 ratios (Figure S22G). M2-biased polymers have been found here to be associated with CO, CC, and CCN molecular fragments, of which GDGDA has several of the CO and CC types. These findings show the possibility of combining high-throughput screening approaches and machine learning to provide frameworks for the identification and design of new polymers with desirable bioinstruction.

For macrophages to exert their function, they initially need to attach to an implant/material. Putative design rules highlighted in this research include that (1) attachment can be being driven by smaller objects, with 15 μm sized octahedra showing preferential attachment for all 3 polarizing materials, and (2) vertex/cone angles of less than 60° increase attachment (Figures 2 and 3).

Across all objects, the linear machine learning model revealed that attachment is influenced by the following within a particular array of a given architecture: having large numbers of small objects and low vertex angles (more pointed object) will increase macrophage attachment, while a large number of spikes and very large areas in between them will decrease macrophage attachment (Figure S14). It is apparent that spikes generally increase macrophage attachment, but comparing spike densities, denser spikes will increase macrophage attachment. Generally, most objects investigated were shown to decrease M2/M1 ratios compared with flat surfaces with a few exceptions (Table S4). These observations allowed us to devise a series of simple, putative design rules for achieving a specific macrophage phenotype (Table S5 and presented visually in Figure 5).

We found that, while chemistry was the main driver of macrophage phenotype, surface-bound objects can have effects on phenotype as well. Cells cultured on BDDA (M1) were generally less receptive to topographical cues, while cells cultured on GPOTA (M0) and GDGDA (M2) were more receptive to modulation by object geometries (e.g., judicious use of spikes can lead to a more M1-dominant macrophage population) (Figure S22). Therefore, a complete design process must combine the rules for attachment and polarization using a combination of object and chemistry to achieve any desired effect. The fact that the phenotype of macrophages cultured on BDDA (M1) remains nearly unchanged, even though macrophages are so plastic and receptive to environmental cues, is an interesting topic for future study. Additionally, the dynamic range of M2/M1 ratios can be compared with cytokine-polarized surface marker levels, as shown in Figure S21A, indicating that much lower M2/M1 are not physiologically relevant.

In summary, we identified key relationships between geometry, materials chemistry, and macrophage behavior using the ChemoArchiChip, illustrating its utility as a new platform for interrogating biological structure-function relationships. From a range of polymer candidates, those that preferentially steer macrophages toward characteristic phenotypes on planar surfaces were chosen for printing with a high-resolution additive manufacturing technique to create polymer objects with previously inaccessible geometries. This allowed us to probe the macrophage attachment/phenotype-object-material relationships. The experiments showed how we can improve cell attachment; e.g., objects with shapes that possessed low vertex angles

led to high macrophage attachment independent of materials chemistry, a function mediated by caveola-dependent endocytosis. This has allowed us to determine how to drive macrophages to specific phenotypes. We saw that materials chemistry is the dominant driver for phenotype but that certain shaped objects, such as tetrahedra, could be used to manipulate attachment or enhance the phenotypic drive of the materials. The next challenge in rational design of immune-instructive geometries for *in vivo* application is investigating how tissue environments will influence the function of specific geometries and chemistries highlighted here.

## EXPERIMENTAL PROCEDURES

### Resource availability

#### *Lead contact*

The lead contact is Morgan Alexander.

#### *Materials availability*

Materials are available upon request from the lead author.

#### *Data and code availability*

All relevant data are available from https://bacterialweb.nottingham.ac.uk/node_list/ under Vassey et al., *Matter* 2022.

### 2PP-based high-throughput formulation and assessment

To achieve systematic sampling of object shapes at length scales broadly equivalent to those of immune cells, we used 2PP (Nanoscribe GT) in a high-throughput, multi-material screening mode. 2PP provided a high-precision 3D array-based platform that allowed structure-function relationships to be probed in a library of micron-scale surface-mounted 3D objects. Optimization of the 2PP formulations for a range of (meth)acrylates is described in detail in Figures S1 and S2. These figures also outline how a multiwell format containing up to 90 different formulations can be used to optimize printing fidelity with a systematic screen of photo-initiator, co-monomers, solvent addition, and 2PP system fabrication parameters.

### ChemoArchiChip preparation

Glass coverslips (Scientific Laboratory Supplies) were cleaned using oxygen plasma (p = 0.3 mbar, 100 W, 1 min). They were immediately transferred into dry toluene (500 mL) under argon. The silane adhesion promotor 3-(trimethoxysilyl) propyl methacrylate (10 mL) was added to the solution, and the reaction mixture was heated to 50°C for 24 h. The slides were then cooled to room temperature and washed twice by sonication with 100 mL of toluene. The slides were then dried under a vacuum in a silicone-free vacuum oven (50°C) for 24 h.

### Surface chemistry selection

In the initial screening of polymers for the macrophage polarization study, polymer micro-arrays were printed on glass slides using methods described previously. Briefly, printing was done using a XYZ3200 dispensing station (Biodot) and metal pins (946MP3B, Arrayit) at 25°C, with oxygen levels below 2,000 ppm and 35% humidity. The monomers used were purchased from Sigma-Aldrich, Scientific Polymers, and Polysciences. Polymerization stock solutions, composed of monomer (50% [v/v]) in dimethylformamide (DMF) with photo-initiator (2,2-dimethoxy-2-phenylacetophenon) (1% [w/v]), were printed onto epoxy-coated slides (Xenopore) dip-coated with poly(2-hydroxyethyl methacrylate) (pHEMA; 4% [w/v]) in ethanol (95% [v/v] in water). 283 homopolymers were printed on a slide in triplicates. Micro-array slides were kept in the vacuum oven (<50 mTorr) for at least 7 days for extraction of

solvent. Slides were then UV sterilized at a wavelength of 245 nm for 20 min and washed in tissue culture-grade phosphate-buffered saline (PBS) before use. Monocytes were seeded on micro-array slides at a density of $1 \times 10^6$ cells/mL with a total medium volume of 5 mL and cultured for 6 days. Cells were then fixed, stained, and imaged for M1 and M2 markers. In this array, cell phenotype was measured as a ratio of surface markers specific for the M1 or M2 phenotype, and the average M2/M1 ratio across 7 donors was calculated for 283 homopolymers. Using the partition around medoids (PAM) data clustering algorithm, polymers were separated based on their M2/M1 values into high, medium, and low M2/M1 value clusters. Excluding medium clusters, high and low clusters (representing M2- and M1-polarizing polymers, respectively) were used to train the supervised machine learning models. By encoding different polymer chemistries with molecular fragments that were directly associated with polymer structure, chemically informative models were provided. This was achieved using the least absolute shrinkage and selection operator (LASSO) feature selection method coupled with machine learning methods. Two-class machine learning models were generated using random forest, multilayer perceptron, and support vector machines models. Based on their M2/M1 ratios and their potential reactivity (where the number of vinyl groups was used as a benchmark; i.e., the greater the number of vinyl groups the greater the potential reactivity), different candidate monomers were chosen as base materials for fabrication.

Monomer solutions of GPOTA (Sigma-Aldrich), BDDA (Sigma-Aldrich), and GDGDA (Sigma-Aldrich) were prepared for printing. PETA (Sigma-Aldrich) was selected as a diluent for BDDA (M1) and GDGDA (M2) to increase printability based on its high polymerization efficiency. Irgacure 369 (2-benzyl-2-(dimethylamino)-4′-morpholinobutyrophenone, Sigma-Aldrich) was chosen as a photoinitiator because its absorption peak is within 1/2 λ of the laser beam, which ensures that Irgacure 369 can be excited to initiate polymerization when a 780-nm laser is applied.

### Microstructure design and fabrication

Computer-aided designs (CAD) for micro-structures were written (a script language containing a list of coordinates) in the commercially available software DeScribe. Briefly, the structures are sliced into several layers by choosing an appropriate slicing thickness, and each layer is filled with lines by choosing hatching distances, contour count, and hatching intervals. A commercial two-photon lithography setup was used for the two-photon fabrication (Nanoscribe Photonic Professional GT). The system is driven by a near infrared spectroscopy (NIR) fiber laser at 780-nm central wavelength, 80-MHz repetition rate, and 120-fs pulse duration. The laser beam was focused by an oil immersion objective lens (1.4 numerical aperture, 63×, 190-μm working distance [WD]). Micro-structures were built by moving the sample position in the xy plane using a galvo mirror and in the z direction using a piezoelectric actuator to move the objective. The laser power was varied between 0% and 100% (50 mW full power), and the scan speed was 20,000 μm/s, both optimized for the respective materials printed. Printing inks (comprised of surface chemistry monomer solution and photoinitiator) were loaded onto a coverslip with immersion oil on the other side of the coverslip. The coverslip was the mounted on the sample holder and inserted into the Nanoscribe system. This system has a capacity of 10 coverslips in the sample holder for multiple sample processing. After processing, the sample on the coverslip was developed in propylene glycol monomethyl ether acetate (PGMEA) and 2-propanol to remove unpolymerized monomer. The sample was then dried in air. Finally, the sample was transferred to an argon-filled glovebox

(mBraun Acrll-Glovebox) maintaining less than 1,000 ppm $O_2$) and irradiated with UV light (2 × 15 W, 365 nm, 15 cm from the samples) for 10 min.

### Scanning electron microscopy

Samples were air dried, mounted to scanning electron microscopy (SEM) stubs affixed with carbon tabs and gold coated via a Polaron E5175 sputter coater at 2.2 Kv for 90 s. Samples were loaded into and imaged with a JEOL6490LV SEM at 10 Kv with a 10-mm WD under a high vacuum.

### Raman spectroscopy

The amount of reacted acrylate groups (RAGs) during polymerization was analyzed by Raman spectroscopy (Horiba-Jobin-Yvon LabRAM). In the crosslinking of acrylate monomers or macromers taking place while printing, the carbon double bonds (C=C) turn into carbon-carbon single bonds (C-C), while the carbon-oxygen double bond (C=O) remains unchanged because it does not participate in the reaction. C=C and C=O bonds give different Raman peaks at 1,635 and 1,723 $cm^{-1}$, respectively. By comparing the unpolymerized formulation and the polymerized structures under Raman, a drop in the intensity of the C=C peaks can be observed as they form C-C bonds, while the intensity of the C=O peak remains the same as before. Therefore, the percentage of RAGs can be calculated using the area under the peaks mentioned before with the following equation:

$$RAG = 1 - [\, A_{C=C}/A_{C=O} \,/\, A'_{C=C}/A'_{C=O} \,],$$

where AC = C/AC = O are the areas under the peaks in polymerized structures, and A'C=C/A'C=O are the peak areas of unpolymerized formulation.

### ToF-SIMS analysis

Time-of-flight secondary ion mass spectrometry (ToF-SIMS) mapping of complex objects was carried out using a 3D OrbiSIMS (Hybrid SIMS) instrument from IONTOF. The ToF-SIMS data were acquired in positive ion polarity mode in delayed extraction mode by raster scanning a 30-keV $Bi_3^+$ primary ion beam (delivering 0.08 pA) of 100 × 100 $\mu m^2$. The ToF analyzer was set with 200-μs cycle time, resulting in a mass range between 0 and 2,233 mass units. All ToF-SIMS intensity maps were produced using the simsMVA software.[42]

Surface ToF-SIMS for the cross-contamination tests was carried out using a ToF-SIMS IV instrument (IONTOF). Secondary ion mass spectra were acquired in positive ion polarity mode using a 25-keV $Bi_3^+$ primary ion beam delivering 0.3 pA. The primary ion beam was raster scanned over different areas, with the total ion dose kept under the static limit of $10^{13}$ ions/$cm^2$. The ToF analyzer was set with 200-μs cycle time, resulting in a mass range between 0 and 3,492 mass units and a low-energy (20 eV) electron flood gun employed to neutralize charge buildup.

Unsupervised machine learning for all datasets was carried out using secondary ion masses as the variables and mapping pixels as observations. For each dataset, Surface Lab 7.1 (IONTOF) was used to perform an automated peak search on the total spectra, restricted only to peaks with an intensity higher than 100 counts and masses between 30 u and 300 u. Dead-time-corrected peak areas were then exported for each observation. Principal-component analysis (PCA) and non-negative matrix factorization (NMF) were performed using the simsMVA software.[42] Prior to PCA and NMF, data were Poisson scaled to account for heteroscedasticity. To create the NMF model from the signal of flat samples, repeat spectra were acquired for

all three GPOTA (M0), GDGDA (M2), and BDDA (M1) formulations as well as for the pre-treated substrate (example reference spectra are shown in Figure S3). The data were arranged in a matrix $\mathbf{M_1}$ with peak intensities in columns and repeats in rows. NMF with 3 endmembers (each representing a "pure" compound) was achieved using a Poisson-based multiplicative update rule algorithm (Figure S3):[43,44]

$$\mathbf{M_1} = \mathbf{W_1 H} + \mathbf{e}$$

where $\mathbf{e}$ is an error matrix, $\mathbf{W_1}$ contains the relative endmember intensity per observation, and $\mathbf{H}$ contains the relative secondary ion peak intensities for each endmember. Upon confirmation that matrix $\mathbf{W_1}$ separated the repeats of reference samples, the pseudo inverse of matrix $\mathbf{H}$ was used to obtain the relative endmember intensities $\mathbf{W_2}$ for the mapping data of complex objects (arranged in a matrix $\mathbf{M_2}$ with pixels in rows and peak intensities in columns):

$$\mathbf{W_2} = \mathbf{M_2 H}\left(\mathbf{H}^{\mathrm{T}}\mathbf{H}\right)$$

## AFM

The MFP-3D standalone atomic force microscope (Oxford Instruments, Asylum Research, CA, USA) was used to obtain force-displacement curves of the polymer samples under air (dry) and water (wet) conditions for Young's modulus (E) calculation. An AFM silicon nitride probe, RTESPA-300 (Bruker Nano, CA, USA) was used. The tip half-conical angle was characterized by measurement of a polystyrene film standard sample (E = 2.7 GPa) with a value of $20.4^\circ \pm 0.2^\circ$, while thermal tuning was used to define the effective spring constant of the cantilever at 82.75 nN/nm. The Derjaguin-Muller-Toporov mathematical model was used to fit the slope of the retracting curve using a least-squares regression line for E calculation.

## Monocyte isolation

Buffy coats from healthy donors were obtained from the National Blood Service (Sheffield, UK) following ethics committee approval (2009/D055). Peripheral blood mononuclear cells (PBMCs) were isolated from heparinized blood by Histopaque-1077 (Sigma-Aldrich) density gradient centrifugation. Monocytes were isolated from PBMCs using the MACS magnetic cell separation system (positive selection with CD14 MicroBeads and LS columns, Miltenyi Biotec) as described previously.[39,45]

## Cell culture

Purified monocytes were suspended in RPMI-1640 medium supplemented with 10% fetal bovine serum (FBS), 2 mM L-glutamine, 100 U/mL penicillin, and 100 μg/mL streptomycin (all from Sigma-Aldrich) (henceforth referred to as "complete medium") and cultured at 300,000 cells $cm^{-1}$ in 6-well polystyrene plates (Corning Life Sciences).

## Immunocytochemistry

For fluorescence analysis, cells cultured on ChemoArchiChips were immunostained using standard procedures. Adherent cells on coverslips were fixed with 4% paraformaldehyde (Bio-Rad) in PBS for 10 min. Fixation and all subsequent steps in this procedure were carried out at room temperature; all washes were carried out with 0.2% Tween 10 (Sigma-Aldrich) in PBS (5 min per wash) except where stated. Following fixation, cells were washed three times and blocked with 1% (w/v) glycine (Fisher Scientific) and 3% (v/v) bovine serum albumin (BSA; Sigma-Aldrich) in PBS for 30 min. Subsequently, cells were washed twice and incubated for 30 min with 5% (v/v) goat serum (Sigma-Aldrich) in PBS to block non-specific antibody binding. Cells were stained with anti-human calprotectin and anti-human mannose receptor incubated for 1 h, washed 3 times, and then incubated for 1 h with the appropriate secondary

antibody at room temperature (for all antibody information, see Table S2). Finally, all cells were stained with SYTOX Deep Red nuclear stain according to the manufacturer's instructions, washed 3 times with PBS and once with $dH_2O$, and then mounted with anti-fade medium (Pro-Long Gold) on a standard microscope slide, followed by imaging using an automated fluorescent confocal microscope (Carl Zeiss).

### Image acquisition

Images were acquired with a Zeiss LSM710 microscope (Carl Zeiss) with a 20× plan-Apochromat/0.8 NA (M27) differential interference contrast (DIC) objective. Zen 2012 software (v.6.0, Carl Zeiss) was used to capture images, and for image stacks, slices were captured at 1-micron intervals. All data were processed using ImageJ (v.1.52p, Java 1.8.0_172 [64 bit]) and ZEN Zeiss LSM 700 imaging software.

### 3D image analysis

A custom ImageJ macro was developed to identify and measure cells attached to the 3D-printed objects, and the phenotype of these cells was determined by fluorescence intensity. The processing and analysis were carried out following these steps. (1) Raw tiff images exported from Zen were imported into ImageJ Fiji. (2) A maximum-intensity projection was created of all fluorescence channels. (3) Background subtraction was carried out (using a rolling ball of 20 pixel). (4) The default thresholding method was used to distinguish the objects and cell signal from the background-thresholding, setting a minimum and maximum pixel intensity range on the selected image that groups all pixels falling within this range and excluding the background. (5) To quantify cells on objects, after application of a threshold, the image from the blue channel (405-nm excitation) was used to determine the object region of interest (ROI) using the native autofluorescence and exclude cells not on the 3D-printed objects. This ROI was dilated 4 times to ensure that peripheral cell attachment was also counted. (6) After application of a threshold, the image of cell nuclei was then combined with the object ROI and subjected to particle analysis to quantify cells only associated within the boundary of the printed object. (7) An outline of the identified cell nuclei within the object ROI was automatically exported as tiff so that it could be compared with the original images. (8) To quantify cell phenotype fluorescence measurements, the identified cell nucleus ROI was dilated 4 times and then redirected to the green (488 nm, M2, mannose receptor) and red channels (561 nm, M1, calprotectin) independently. Particle analysis was carried out in each channel to generate area, standard deviation, mean, and median gray values. Because of material autofluorescence by GDGDA (M2) objects, an initial step was added, consisting of an machine learning-based annotation and segmentation tool called APEER (Carl Zeiss). Example images were first annotated for the cell nuclei and object and then applied for all GDGDA (M2) images and segmented into cell nucleus and background masks. The cell nucleus mask was then referred to during step 4 in the aforementioned custom ImageJ macro.

All datasets were run through batch analysis, and the results were automatically exported as a text file. Data were exported to Microsoft Excel and was visualized using GraphPad Prism v.9.0.2 (64 bit) (https://www.graphpad.com).

### Data modeling

Design parameters as well as radiomics descriptors provided a total of 44 descriptors used for computational modeling. Radiomics descriptors were obtained by converting the CAD files for the objects into nearly raw raster data (nrrd) file formats, which were processed by the "pyradiomics" Python package (v.3.0.1). Table S1 shows the full list of descriptors obtained. Multiple linear regression with

expectation maximization (MLREM) and random forest regression (from package "scikit-learn" with default parameters) using bootstrapping (50 sample sets without replacement) implemented in Python were used to identify linear and non-linear structure activity relationships for macrophage attachment, polarization (modeled as log(M2/M1), positive for anti-inflammatory and negative for M1), and polarization in synergy with attachment (using a composite variable log(M2/M1) × attachment, larger positive for high attachment M2 and larger negative for M1 high attachment). The 1-hot descriptor approach is commonly used in modeling studies to indicate the presence or absence of a feature; in this case the presence of a particular chemistry is denoted by a 1 in the appropriate cell, with all other cells containing 0. This allows the feature selection algorithms and machine learning models to identify the chemistries and topography descriptors that have the largest impact on biological responses. The random forest machine learning method was applied to generate non-linear relationships between the objects and macrophage polarization responses using the descriptors listed in Table S1.[42] The random forest module from scikit-learn was used with default parameters in Python v.3.7. Seventy percent of each bacterial attachment dataset was used to train the model, and 30% was kept aside to determine the predictive power of the model. The average of 50 runs using bootstrapping without replacement was used to evaluate the model.

### Attachment inhibition

To elucidate the mechanism of macrophage attachment to GPOTA (M0) printed ChemoArchiChips, several inhibitors—cytochalasin-D (2 μM), which prevents caveola- and clathrin-mediated endocytosis by blocking actin polymerization; dynasore (80 μM), which inhibits dynamin-dependent endocytosis; genistein (80 μM), which inhibits caveola-mediated endocytosis; chlorpromazine (80 μM), which inhibits clathrin-mediated endocytosis by preventing assembly and disassembly of clathrin lattices on cell surfaces and on endosomes; and blebbistatin (50 μM), which inhibits myosin II in vesicle fission—were added to the culture of macrophages 0.5 h prior to culture on Chemo ArchiChips before being cultured for a further 72 h. Cell attachment was quantified using the high-throughput confocal imaging and analysis method described above.

### Statistics and reproducibility

An unpaired t test was used to analyze the difference between two groups and a one-way analysis of variance (ANOVA) among multiple groups with a minimum confidence interval of 95%. All data are presented as the mean ± standard deviation (SD), as indicated in the experiments. The p values were calculated by Prism software (GraphPad) and regarded as significant when less than 0.05.

## SUPPLEMENTAL INFORMATION

Supplemental information can be found online at https://doi.org/10.1016/j.matt.2023.01.002.

## ACKNOWLEDGMENTS

We thank Nicola Weston at the Nanoscale and Microscale Research Center (NMRC; University of Nottingham) for technical assistance with electron microscopy. This study was supported by the EPSRC, who are gratefully acknowledged for Next Generation Biomaterials Discovery Program Grant funding (EP/N006615/1) and Enabling Next Generation Additive Manufacturing Program Grant funding (EP/P031684/1) that supported this work. The image analysis for GDGDA was supported by the APEER annotation and segmentation machine learning tool by Carl Zeiss, and

L.K. introduced this and its interpretation into the manuscript. Overview schematics were generated in BioRender.

## AUTHOR CONTRIBUTIONS

M.V., concept, cell culture experiments, data interpretation, image analysis, and writing; L.M., concept, 2PP printing, and writing; L.K., image analysis, data interpretation, and writing; C.M., initial screening and cell culture screening experiments; G.F.T., ToF-SIMS analysis; G.P.F., machine learning; F.P., AFM analysis; J.H., 2PP printing files; R.M. and S.R., image analysis support; Q.H., 2PP proof-of-concept studies; D.A.W., D.J.I., R.H., A.M.G., R.W., and M.R.A., concept, supervision, funding and editing of the manuscript.

## DECLARATION OF INTERESTS

The authors hold a patent application related to this work (UK Patent Application GB2217458.5).

Received: July 21, 2022
Revised: November 7, 2022
Accepted: January 3, 2023
Published: January 23, 2023

## REFERENCES

1. Serruys, P.W., Ormiston, J.A., Onuma, Y., Regar, E., Gonzalo, N., Garcia-Garcia, H.M., Nieman, K., Bruining, N., Dorange, C., Miquel-Hébert, K., et al. (2009). A bioabsorbable everolimus-eluting coronary stent system (ABSORB): 2-year outcomes and results from multiple imaging methods. Lancet *373*, 897–910. https://doi.org/10.1016/S0140-6736(09)60325-1.

2. Nichols, S.P., Koh, A., Storm, W.L., Shin, J.H., and Schoenfisch, M.H. (2013). Biocompatible materials for continuous glucose monitoring devices. Chem. Rev. *113*, 2528–2549. https://doi.org/10.1021/cr300387j.

3. Kurtz, S., Ong, K., Lau, E., Mowat, F., and Halpern, M. (2007). Projections of primary and revision hip and knee arthroplasty in the United States from 2005 to 2030. J. Bone Joint Surg. Am. *89*, 780–785. https://doi.org/10.2106/JBJS.F.00222.

4. Abu-Amer, Y., Darwech, I., and Clohisy, J.C. (2007). Aseptic loosening of total joint replacements: mechanisms underlying osteolysis and potential therapies. Arthritis Res. Ther. *9*, S6. https://doi.org/10.1186/ar2170.

5. Gallo, J., Goodman, S.B., Konttinen, Y.T., Wimmer, M.A., and Holinka, M. (2013). Osteolysis around total knee arthroplasty: a review of pathogenetic mechanisms. Acta Biomater. *9*, 8046–8058. https://doi.org/10.1016/j.actbio.2013.05.005.

6. Hubbell, J.A., and Langer, R. (2013). Translating materials design to the clinic. Nat. Mater. *12*, 963–966. https://doi.org/10.1038/nmat3788.

7. Anderson, J.M., Rodriguez, A., and Chang, D.T. (2008). Foreign body reaction to biomaterials. Semin. Immunol. *20*, 86–100. https://doi.org/10.1016/j.smim.2007.11.004.

8. Cobelli, N., Scharf, B., Crisi, G.M., Hardin, J., and Santambrogio, L. (2011). Mediators of the inflammatory response to joint replacement devices. Nat. Rev. Rheumatol. *7*, 600–608. https://doi.org/10.1038/nrrheum.2011.128.

9. Sussman, E.M., Halpin, M.C., Muster, J., Moon, R.T., and Ratner, B.D. (2014). Porous implants modulate healing and induce shifts in local macrophage polarization in the foreign body reaction. Ann. Biomed. Eng. *42*, 1508–1516. https://doi.org/10.1007/s10439-013-0933-0.

10. Doloff, J.C., Veiseh, O., Vegas, A.J., Tam, H.H., Farah, S., Ma, M., Li, J., Bader, A., Chiu, A., Sadraei, A., et al. (2017). Colony stimulating factor-1 receptor is a central component of the foreign body response to biomaterial implants in rodents and non-human primates. Nat. Mater. *16*, 671–680. https://doi.org/10.1038/nmat4866.

11. Jain, N., and Vogel, V. (2018). Spatial confinement downsizes the inflammatory response of macrophages. Nat. Mater. *17*, 1134–1144. https://doi.org/10.1038/s41563-018-0190-6.

12. McWhorter, F.Y., Wang, T., Nguyen, P., Chung, T., and Liu, W.F. (2013). Modulation of macrophage phenotype by cell shape. Proc. Natl. Acad. Sci. USA *110*, 17253–17258. https://doi.org/10.1073/pnas.1308887110.

13. Veiseh, O., Doloff, J.C., Ma, M., Vegas, A.J., Tam, H.H., Bader, A.R., Li, J., Langan, E., Wyckoff, J., Loo, W.S., et al. (2015). Size- and shape-dependent foreign body immune response to materials implanted in rodents and non-human primates. Nat. Mater. *14*, 643–651. https://doi.org/10.1038/nmat4290.

14. Vassey, M.J., Figueredo, G.P., Scurr, D.J., Vasilevich, A.S., Vermeulen, S., Carlier, A., Luckett, J., Beijer, N.R.M., Williams, P., Winkler, D.A., et al. (2020). Immune modulation by design: using topography to control human monocyte attachment and macrophage differentiation. Adv. Sci. *7*, 1903392. https://doi.org/10.1002/advs.201903392.

15. Rostam, H.M., Fisher, L.E., Hook, A.L., Burroughs, L., Luckett, J.C., Figueredo, G.P., Mbadugha, C., Teo, A.C., Latif, A., Kämmerling, L., et al. (2020). Immune-instructive polymers control macrophage phenotype and modulate the foreign body response in vivo. Matter *2*, 1564–1581. https://doi.org/10.1016/j.matt.2020.03.018.

16. Champion, J.A., and Mitragotri, S. (2006). Role of target geometry in phagocytosis. Proc. Natl. Acad. Sci. USA *103*, 4930–4934. https://doi.org/10.1073/pnas.0600997103.

17. Milton, J.M. (1992). Poly(Ethylene Glycol) Chemistry: Biotechnical and Biomedical Applications (Springer US). https://doi.org/10.1007/978-1-4899-0703-5.

18. Hucknall, A., Rangarajan, S., and Chilkoti, A. (2009). In pursuit of zero: polymer brushes that resist the adsorption of proteins. Adv. Mater. *21*, 2441–2446. https://doi.org/10.1002/adma.200900383.

19. Chapman, D. (1993). Biomembranes and new hemocompatible materials. Langmuir *9*, 39–45. https://doi.org/10.1021/la00025a012.

20. Liu, Q., Chiu, A., Wang, L.-H., An, D., Zhong, M., Smink, A.M., de Haan, B.J., de Vos, P., Keane, K., Vegge, A., et al. (2019). Zwitterionically modified alginates mitigate cellular overgrowth for cell encapsulation. Nat. Commun. *10*, 5262. https://doi.org/10.1038/s41467-019-13238-7.

21. Li, B., Yuan, Z., Jain, P., Hung, H.C., He, Y., Lin, X., McMullen, P., and Jiang, S. (2020). De novo design of functional zwitterionic biomimetic material for immunomodulation. Sci. Adv. *6*,

eaba0754. https://doi.org/10.1126/sciadv.aba0754.

22. Vegas, A.J., Veiseh, O., Doloff, J.C., Ma, M., Tam, H.H., Bratlie, K., Li, J., Bader, A.R., Langan, E., Olejnik, K., et al. (2016). Combinatorial hydrogel library enables identification of materials that mitigate the foreign body response in primates. Nat. Biotechnol. *34*, 345–352. https://doi.org/10.1038/nbt.3462.

23. Vegas, A.J., Veiseh, O., Gürtler, M., Millman, J.R., Pagliuca, F.W., Bader, A.R., Doloff, J.C., Li, J., Chen, M., Olejnik, K., et al. (2016). Long-term glycemic control using polymer-encapsulated human stem cell-derived beta cells in immune-competent mice. Nat. Med. *22*, 306–311. https://doi.org/10.1038/nm.4030.

24. Chen, S., Jones, J.A., Xu, Y., Low, H.Y., Anderson, J.M., and Leong, K.W. (2010). Characterization of topographical effects on macrophage behavior in a foreign body response model. Biomaterials *31*, 3479–3491. https://doi.org/10.1016/j.biomaterials.2010.01.074.

25. Luu, T.U., Gott, S.C., Woo, B.W.K., Rao, M.P., and Liu, W.F. (2015). Micro- and nanopatterned topographical cues for regulating macrophage cell shape and phenotype. ACS Appl. Mater. Interfaces *7*, 28665–28672. https://doi.org/10.1021/acsami.5b10589.

26. Möller, J., Luehmann, T., Hall, H., and Vogel, V. (2012). The race to the pole: how high-aspect ratio shape and heterogeneous environments limit phagocytosis of filamentous Escherichia coli bacteria by macrophages. Nano Lett. *12*, 2901–2905. https://doi.org/10.1021/nl3004896.

27. McWhorter, F.Y., Davis, C.T., and Liu, W.F. (2015). Physical and mechanical regulation of macrophage phenotype and function. Cell. Mol. Life Sci. *72*, 1303–1316. https://doi.org/10.1007/s00018-014-1796-8.

28. Wójciak-Stothard, B., Madeja, Z., Korohoda, W., Curtis, A., and Wilkinson, C. (1995). Activation of macrophage-like cells by multiple grooved substrata. Topographical control of cell behaviour. Cell Biol. Int. *19*, 485–490. https://doi.org/10.1006/cbir.1995.1092.

29. Mikulskis, P., Alexander, M.R., and Winkler, D.A. (2019). Toward interpretable machine learning models for materials discovery. Adv. Intell. Syst. *1*, 1900045. ARTN 1900045. https://doi.org/10.1002/aisy.201900045.

30. Bartneck, M., Schulte, V.A., Paul, N.E., Diez, M., Lensen, M.C., and Zwadlo-Klarwasser, G. (2010). Induction of specific macrophage subtypes by defined micro-patterned structures. Acta Biomater. *6*, 3864–3872. https://doi.org/10.1016/j.actbio.2010.04.025.

31. Kumar, G.A., Karmakar, J., Mandal, C., and Chattopadhyay, A. (2019). Leishmania donovani internalizes into host cells via caveolin-mediated endocytosis. Sci. Rep. *9*, 12636. https://doi.org/10.1038/s41598-019-49007-1.

32. Shin, J.S., and Abraham, S.N. (2001). Cell biology. Caveolae–not just craters in the cellular landscape. Science *293*, 1447–1448. https://doi.org/10.1126/science.1061079.

33. Wang, J., Chen, H.J., Hang, T., Yu, Y., Liu, G., He, G., Xiao, S., Yang, B.R., Yang, C., Liu, F., et al. (2018). Physical activation of innate immunity by spiky particles. Nat. Nanotechnol. *13*, 1078–1086. https://doi.org/10.1038/s41565-018-0274-0.

34. McNamara, L.E., Burchmore, R., Riehle, M.O., Herzyk, P., Biggs, M.J.P., Wilkinson, C.D.W., Curtis, A.S.G., and Dalby, M.J. (2012). The role of microtopography in cellular mechanotransduction. Biomaterials *33*, 2835–2847. https://doi.org/10.1016/j.biomaterials.2011.11.047.

35. Moerke, C., Mueller, P., and Nebe, B. (2016). Attempted caveolae-mediated phagocytosis of surface-fixed micro-pillars by human osteoblasts. Biomaterials *76*, 102–114. https://doi.org/10.1016/j.biomaterials.2015.10.030.

36. Gopal, S., Chiappini, C., Penders, J., Leonardo, V., Seong, H., Rothery, S., Korchev, Y., Shevchuk, A., and Stevens, M.M. (2019). Porous silicon nanoneedles modulate endocytosis to deliver biological payloads. Adv. Mater. *31*, e1806788. https://doi.org/10.1002/adma.201806788.

37. von Erlach, T.C., Bertazzo, S., Wozniak, M.A., Horejs, C.-M., Maynard, S.A., Attwood, S., Robinson, B.K., Autefage, H., Kallepitis, C., Del Río Hernández, A., et al. (2018). Cell-geometry-dependent changes in plasma membrane order direct stem cell signalling and fate. Nat. Mater. *17*, 237–242. https://doi.org/10.1038/s41563-017-0014-0.

38. Brown, B.N., Ratner, B.D., Goodman, S.B., Amar, S., and Badylak, S.F. (2012). Macrophage polarization: an opportunity for improved outcomes in biomaterials and regenerative medicine. Biomaterials *33*, 3792–3802. https://doi.org/10.1016/j.biomaterials.2012.02.034.

39. Rostam, H.M., Singh, S., Salazar, F., Magennis, P., Hook, A., Singh, T., Vrana, N.E., Alexander, M.R., and Ghaemmaghami, A.M. (2016). The impact of surface chemistry modification on macrophage polarisation. Immunobiology *221*, 1237–1246. https://doi.org/10.1016/j.imbio.2016.06.010.

40. Lundberg, S.M., and Lee, S.-I. (2017). A unified approach to interpreting model predictions. Preprint at ArXiv. *abs/1705.07874*.

41. Burroughs, L., Amer, M.H., Vassey, M., Koch, B., Figueredo, G.P., Mukonoweshuro, B., Mikulskis, P., Vasilevich, A., Vermeulen, S., Dryden, I.L., et al. (2021). Discovery of synergistic material-topography combinations to achieve immunomodulatory osteoinductive biomaterials using a novel in vitro screening method: the ChemoTopoChip. Biomaterials *271*, 120740. https://doi.org/10.1016/j.biomaterials.2021.120740.

42. Trindade, G.F., Abel, M.-L., and Watts, J.F. (2018). simsMVA: a tool for multivariate analysis of ToF-SIMS datasets. Chemometr. Intell. Lab. Syst. *182*, 180–187. https://doi.org/10.1016/j.chemolab.2018.10.001.

43. Lee, D.D., and Seung, H.S. (1999). Learning the parts of objects by non-negative matrix factorization. Nature *401*, 788–791. https://doi.org/10.1038/44565.

44. Lee, D.D., and Seung, H.S. (2000). Algorithms for non-negative matrix factorization. In Proceedings of the 13th International Conference on Neural Information Processing Systems (MIT Press).

45. Rostam, H.M., Reynolds, P.M., Alexander, M.R., Gadegaard, N., and Ghaemmaghami, A.M. (2017). Image based Machine Learning for identification of macrophage subsets. Sci. Rep. *7*, 3521. https://doi.org/10.1038/s41598-017-03780-z.